remote sensing

MDPI

Article

Direction-of-Arrival Estimation for a Floating HFSWR Through Iterative Adaptive Beamforming of Focusing Concept

Xianzhou Yi [1], Min Qu [1], Zhihui Li [1], Shuyun Shi [1], Li Wang [2,*], Xiongbin Wu [3] and Liang Yu [3]

[1] College of Electronic Engineering, National University of Defense Technology, Hefei 230037, China; xianzhouyi@whu.edu.cn (X.Y.); qumin45@nudt.edu.cn (M.Q.); lizhihui20@nudt.edu.cn (Z.L.); shishuyun21@nudt.edu.cn (S.S.)
[2] College of Meteorology and Oceanography, National University of Defense Technology, Changsha 410073, China
[3] School of Earth and Space Science Technology, Wuhan University, Wuhan 430072, China; xbwu@whu.edu.cn (X.W.); liang_yu@whu.edu.cn (L.Y.)
* Correspondence: warren@whu.edu.cn; Tel.: +86-158-0277-1605

Abstract: Floating high-frequency surface-wave radar provides an effective solution to widening the range of detection by such radar systems. However, for high-frequency radars with long coherence integration times, the yaw angle variations during this period can have a significant impact on the accuracy of direction-of-arrival estimation. Although adaptive beamforming methods are applicable to yaw angle compensation, their effectiveness can be significantly reduced when the measured distortion of antenna patterns is considered. To solve this problem, an iterative adaptive beamforming of focusing concept is proposed in this paper to compensate for yaw rotation. Firstly, an adaptive beamforming technique, called balanced-focusing pseudo-fixed beamforming, is developed to improve the ability of beam shape control by shortening the constraint range of the azimuth. Then, the shortened focusing range is determined by one iterative strategy that iteratively reduces the focusing length and selects the focusing center. The simulation results demonstrate that the proposed algorithm is applicable to significantly improve the precision and stability of direction-of-arrival estimation. This algorithm is also validated against the results obtained from two cooperative signals and ship echoes in a field experiment.

Keywords: direction-of-arrival estimation; floating high-frequency surface-wave radar; yaw compensation; adaptive beamforming

check for updates

Academic Editor: Kaoru Ichikawa

Received: 18 January 2025
Revised: 18 March 2025
Accepted: 27 March 2025
Published: 29 March 2025

Citation: Yi, X.; Qu, M.; Li, Z.; Shi, S.; Wang, L.; Wu, X.; Yu, L. Direction-of-Arrival Estimation for a Floating HFSWR Through Iterative Adaptive Beamforming of Focusing Concept. *Remote Sens.* **2025**, *17*, 1220. https://doi.org/10.3390/rs17071220

Copyright: © 2025 by the authors. Licensee MDPI, Basel, Switzerland. This article is an open access article distributed under the terms and conditions of the Creative Commons Attribution (CC BY) license (https://creativecommons.org/licenses/by/4.0/).

1. Introduction

High-frequency surface-wave radar (HFSWR) has already been widely used for various purposes related to ocean surveillance, such as ocean dynamics measurement [1–5] and object detection and tracking [6–8]. By mounting one high-frequency radar on a floating platform, maneuverability can be enhanced, and valuable coastal land can be saved. However, Doppler and spatial spectrum modulation, caused by the six-degree-of-freedom (DOF) motions, tends to compromise the coherent integration of a signal and further reduce the accuracy of parameter estimations. For one floating HFSWR, horizontal 2-DOF translations and 3-DOF rotations can make the Doppler spectrum broaden [9], shift [10] or even have multiple peaks [11,12]. Three-DOF rotations can further cause spatial spectrum modulation, i.e., the steering vector keeps varying during one coherent integration time (CIT), which reduces the precision and the stability of direction-of-arrival (DOA) estimation [13]. The pitch and roll motions of the floating platform are similar to each other and both oscillate

around the ocean surface with small oscillation amplitudes, while the yaw variations can change incrementally, and the range of the yaw may be very large. Regarding the 3-DOF rotations, many studies [14–16] have indicated that the yaw is the most significant contributor to spatial spectrum modulation. This paper aims to compensate for yaw rotation and further improve the performance of DOA estimation. To achieve this purpose, there are two mainstream methods used for yaw compensation: the frequency-domain method and the time-domain method.

The frequency-domain method involves conducting yaw compensation after a double-fast Fourier transformation through the selection of one suitable reference yaw angle. Yang et al. [14] used the weighted average of the yaw angles during one CIT to demonstrate that this method can improve the precision of DOA estimation. Nevertheless, this approach fails to eliminate the DOA bias in theory.

The time-domain method requires that yaw compensation is conducted for each sweep period of the radar, with three different ideas involved: steering vector compensation, digital beamforming (DBF), and adaptive beamforming. The first idea necessitates the construction of a steering vector based on real-time six DOF movements, followed by compensation for the varying steering vector [17]. In theory, the motion compensation method can eliminate the negative influence of yaw rotation on the direction-finding process. The second idea is to conduct digital beamforming according to the real-time yaw angle. Ji et al. [18] achieved compensation for non-uniform linear motion, the weight vector of which is supposed to be the real-time steering vector of a specific direction. As for the true direction of an object, it can be determined when the power output reaches its maximum. However, this renders spatial spectrum estimation methods inapplicable, such as multiple signal classification (MUSIC) [19] and a minimum variance distortionless response [20]. The third idea is adaptive beamforming, which makes the real-time beam shapes and reference beam shapes as identical to each other as possible while converting data from antenna channels into beam channels. This makes the spatial spectrum estimation methods applicable in the beam domain. Yi et al. [13] proposed an adaptive channel conversion method, namely, global pseudo-fixed beamforming (GPFB), which is implemented by minimizing the errors between the real-time beams and reference beams. GPFB is effective in reducing the DOA bias when yaw rotation is obvious. Furthermore, a comprehensive, adaptive beamforming method called balanced global pseudo-fixed beamforming (BGPFB) [21] has been proposed to avoid the signal-to-noise ratio (SNR) caused by adaptive beamforming, further demonstrating the potential of radar-based methods in complex environments.

Adaptive beamforming can be performed to maintain the channel information, suggesting that the data after yaw compensation can use the methods for phased array, which is infeasible with steering vector compensation or digital beamforming. However, the ability of beam shape control is insufficient when considering the measured antenna distortions [13]. To avoid the SNR loss caused by adaptive beamforming, the ability of beam shape control should be further compromised for BGPFB, which results in larger DOA errors of cooperative signals [21]. In this paper, the compensation performance is further improved by putting forward one focusing adaptive beamforming algorithm, which can be used to perform adaptive beamforming in a much smaller azimuth scale. This method can significantly enhance the capability of beam shape control while avoiding SNR loss. To gain the focusing azimuth scale, one iterative strategy that aims to determine the center and length of the azimuth scale is also proposed.

The remainder of this paper is structured as follows. Section 2 elaborates on the proposed iterative adaptive beamforming of focusing concept. Section 3 presents the simulation results of DOA estimation, with consideration given to the measured antenna distortions. Section 4 presents the field experiment results of the DOA estimation for

cooperative signals and ship echoes. At last, the discussions and conclusions are drawn in Sections 5 and 6, respectively.

2. Methodology

This section starts by establishing the echo signal model for a floating HFSWR, with a focus on the analysis of the part related to DOA estimation. Then, an introduction is made regarding the yaw compensation scheme based on the developed adaptive beamforming methods, GPFB and BGPFB, and their limitations in practice. Finally, an iterative adaptive beamforming of the focusing concept is proposed, and the corresponding DOA estimation process is detailed.

2.1. Signal Model of Floating HFSWR

Figure 1 shows the motions in six degrees of freedom for a floating platform. Fixedly connected with the floating platform, the X-Y-Z coordinate system moves with the platform, which is called the motion coordinate system. Instead of moving with the platform, the E-N-S (east-north-sky) coordinate system is always stationary, which is called the reference coordinate system. The x_f, y_f and z_f denote the eastward, northward, and skyward displacements, respectively. The φ_f, Ψ_f and Φ_f denote the yaw, pitch, and roll angles, respectively. Thus, the received signal is:

$$\boldsymbol{r}(t) = \boldsymbol{a}\left(\theta, \Theta,\ \varphi_f, \Phi_\mathrm{f}, \Psi_\mathrm{f}\right) s(t, x_\mathrm{f}, y_\mathrm{f}, z_\mathrm{f}) + \boldsymbol{n}(t) \tag{1}$$

where $\boldsymbol{n}(t)$ represents the noise vector of the receiving array, θ denotes the azimuthal angle of the target, which is also the DOA that needs to be estimated in this paper, Θ denotes the pitch angles of the target, $s(t, x_\mathrm{f}, y_\mathrm{f}, z_\mathrm{f})$ denotes the received waveform of the target at the coordinate origin, and $\boldsymbol{a}\left(\theta, \Theta,\ \varphi_f, \Phi_\mathrm{f}, \Psi_\mathrm{f}\right)$ refers to the real-time steering vector.

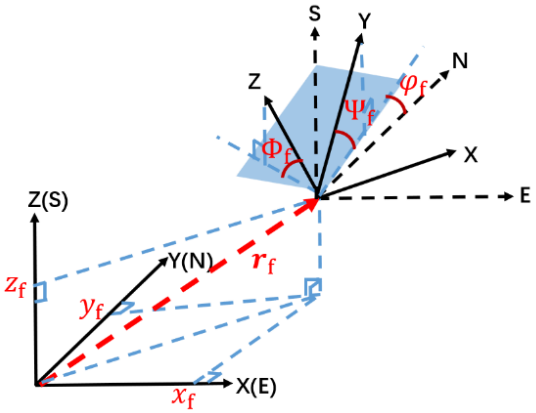

Figure 1. Motions in six degrees of freedom for a floating platform.

$s(t, x_\mathrm{f}, y_\mathrm{f}, z_\mathrm{f})$ can be expressed as:

$$s(t, x_\mathrm{f}, y_\mathrm{f}, z_\mathrm{f}) = s_0\left(t - \tau\left(t, x_\mathrm{f}, y_\mathrm{f}, z_\mathrm{f}, \varphi_f, \Phi_\mathrm{f}, \Psi_\mathrm{f}\right)\right) \tag{2}$$

where $s_0(t)$ represents the transmit waveform of radar, and $\tau\left(t, x_\mathrm{f}, y_\mathrm{f}, z_\mathrm{f}, \varphi_f, \Phi_\mathrm{f}, \Psi_\mathrm{f}\right)$ denotes the real-time delay of the target based on the far-field model, which can be expressed as:

$$\tau\left(t, x_\mathrm{f}, y_\mathrm{f}, z_\mathrm{f}, \varphi_f, \Phi_\mathrm{f}, \Psi_\mathrm{f}\right) = \frac{2\left(\mathrm{R}_0 + v_r t + \boldsymbol{r}_\mathrm{f}^\mathrm{T}\overline{\boldsymbol{n}}(\theta, \Theta)\right) + \boldsymbol{r}_\mathrm{t}^\mathrm{T}\boldsymbol{R}(\varphi_\mathrm{f}, \Psi_\mathrm{f}, \Phi_\mathrm{f})\overline{\boldsymbol{n}}(\theta, \Theta)}{c} \tag{3}$$

where $(\cdot)^{\mathrm{T}}$ denotes the transpose of a vector or matrix, R_0 indicates the initial distance of the target from the radar, v_r is referred to as the radial velocity, $\boldsymbol{r}_{\mathrm{f}} = (x_{\mathrm{f}}, y_{\mathrm{f}}, z_{\mathrm{f}})^{\mathrm{T}}$ denotes the real-time translational vector of the platform, $\boldsymbol{r}_{\mathrm{t}} = (x_{\mathrm{t}}, y_{\mathrm{t}}, z_{\mathrm{t}})^{\mathrm{T}}$ indicates the coordinate vector of the transmit antenna, $\overline{\boldsymbol{n}}(\theta, \Theta)$ denotes the unit vector in the direction of the target, where the θ and Θ represent the azimuth and pitch angles of the target, respectively, c is the velocity of the electromagnetic wave, and $\boldsymbol{R}(\varphi_{\mathrm{f}}, \Psi_{\mathrm{f}}, \Phi_{\mathrm{f}})$ denotes the matrix of platform rotation.

$\overline{\boldsymbol{n}}(\theta, \Theta)$ can be obtained as:

$$\overline{\boldsymbol{n}}(\theta, \Theta) = \begin{pmatrix} \cos(\theta)\cos(\Theta) \\ \sin(\theta)\cos(\Theta) \\ \sin(\Theta) \end{pmatrix}. \tag{4}$$

$\boldsymbol{R}(\varphi_{\mathrm{f}}, \Psi_{\mathrm{f}}, \Phi_{\mathrm{f}})$ can be obtained as:

$$\boldsymbol{R}(\varphi_{\mathrm{f}}, \Psi_{\mathrm{f}}, \Phi_{\mathrm{f}}) = \begin{pmatrix} \cos(\Phi_{\mathrm{f}}) & 0 & -\sin(\Phi_{\mathrm{f}}) \\ 0 & 1 & 0 \\ \sin(\Phi_{\mathrm{f}}) & 0 & \cos(\Phi_{\mathrm{f}}) \end{pmatrix} \begin{pmatrix} 1 & 0 & 0 \\ 0 & \cos(\Psi_{\mathrm{f}}) & \sin(\Psi_{\mathrm{f}}) \\ 0 & -\sin(\Psi_{\mathrm{f}}) & \cos(\Psi_{\mathrm{f}}) \end{pmatrix} \begin{pmatrix} \cos(-\varphi_{\mathrm{f}}) & \sin(-\varphi_{\mathrm{f}}) & 0 \\ -\sin(-\varphi_{\mathrm{f}}) & \cos(-\varphi_{\mathrm{f}}) & 0 \\ 0 & 0 & 1 \end{pmatrix}. \tag{5}$$

The time delay can be used to describe the modulation effects of the target distance from the radar, the motions of the target, the translations of the platform, and the rotations of the transmitting antenna. These modulations are consistent for each receiving antenna, exerting no effect on the receiving array goniometry. The most significant effect on the receiving array goniometry is caused by its steering vector, which can be expressed as:

$$\boldsymbol{a}\left(\theta, \Theta, \varphi_f, \Phi_{\mathrm{f}}, \Psi_{\mathrm{f}}\right) = e^{\mathrm{i}k_0[\boldsymbol{C}_r \boldsymbol{R}(\varphi_{\mathrm{f}}, \Psi_{\mathrm{f}}, \Phi_{\mathrm{f}})\overline{\boldsymbol{n}}(\theta, \Theta)]} \tag{6}$$

where $\mathrm{i}\left(\mathrm{i}^2 = -1\right)$ represents the imaginary part unit, k_0 is the wave number of the electromagnetic wave, and $\boldsymbol{C}_r$ indicates the receiving antenna coordinate matrix, each row of which represents the coordinates of one receiving antenna. When the target observed is on the sea surface, Θ can be considered as zero. Moreover, the rotation characteristics of one floating platform are taken into account, which means its pitch and roll angles are restricted. The vibration amplitude of the two types of rotation is limited. Therefore, the impact of such rotations on the target direction measurement on the horizontal plane is insignificant. Hence, the pitch and roll are ignored in this paper. Therefore, $\boldsymbol{a}\left(\theta, \Theta, \varphi_f, \Phi_{\mathrm{f}}, \Psi_{\mathrm{f}}\right)$ can be simplified as:

$$\boldsymbol{a}\left(\theta, \varphi_f\right) = e^{\mathrm{i}k_0[\boldsymbol{C}_r \boldsymbol{R}(\varphi_{\mathrm{f}}, 0, 0)\overline{\boldsymbol{n}}(\theta, 0)]}. \tag{7}$$

Figure 2 shows a floating radar receiving echoes on the surface under this simplified scenario. An eight-element uniform circular array is used in this figure, which is the array used in the following simulations and field experiments. The center of the circle indicates the center of the receiving array. For a target in the east, when the yaw angle changes from zero degrees to φ_f, the angle of the target measured by the receiving array is expected to change from zero degrees to φ_f. For a long CIT, the estimated angle should be an uncertain value on a large scale. Regarding the special characteristics of HFSWR's working band and working environment, its CIT often takes tens of seconds or even several minutes. For example, when the CIT is five minutes, the range of the yaw angle variation in one field experiment may reach as high as eighty degrees [13].

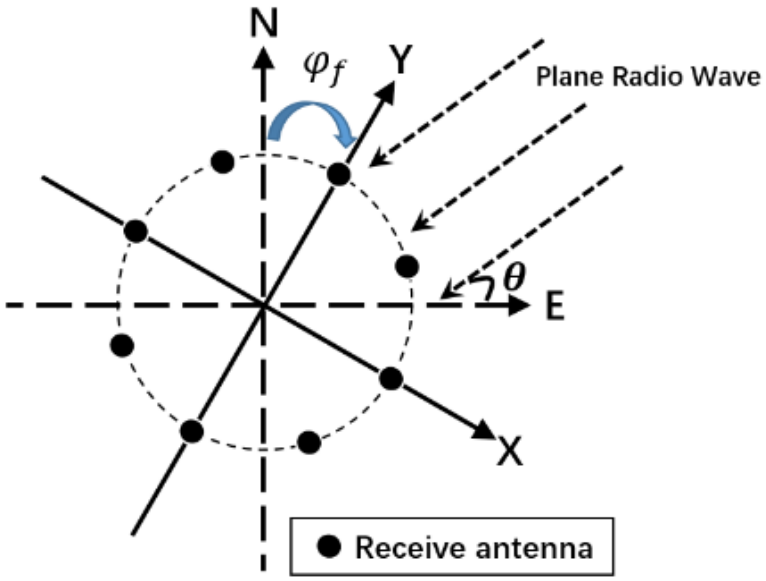

Figure 2. The sketch map of an array receiving a far-field plane wave from the direction of θ when the yaw angle is φ_f. When $\varphi_f = 0$, the X-Y coordinate system superposes the E-N coordinate system.

2.2. Adaptive Beamforming for Yaw Compensation and Its Limitations

The basic concept of adaptive beamforming for yaw compensation is to perform beamforming according to the real-time yaw angle. Through this process, the antenna channel data are transformed into beam channel data, with the steering vector in the beam domain unchanged to the ground. Therefore, the aim to compensate for the adverse effect of yaw angle changes on the angle estimation can be realized. The process of channel data conversion is expressed as:

$$\boldsymbol{r_B}(t) = \boldsymbol{W}^{\mathrm{H}}\left(\varphi_f\right)\boldsymbol{r}(t) \tag{8}$$

where $\boldsymbol{W}\left(\varphi_f\right)$ denotes the weight matrix according to the real-time yaw angle, each column of which represents one weight vector, $(\cdot)^{\mathrm{H}}$ denotes the conjugate transpose of a vector or matrix, and $\boldsymbol{r}(t)$ are the received data in the antenna domain, as discussed in (1). A total of K beam channels should be obtained, which is also the number of receive antennas. $\boldsymbol{W}\left(\varphi_f\right)$ can be expressed as:

$$\boldsymbol{W}\left(\varphi_f\right) = \left(\boldsymbol{w}_1\left(\varphi_f\right), \boldsymbol{w}_2\left(\varphi_f\right), \ldots, \boldsymbol{w}_{\mathrm{K}}\left(\varphi_f\right)\right). \tag{9}$$

Therefore, the steering vector in the beam domain is obtained as:

$$\boldsymbol{a}_B\left(\theta, \varphi_f\right) = \boldsymbol{W}^{\mathrm{H}}\left(\varphi_f\right)\boldsymbol{a}\left(\theta, \varphi_f\right). \tag{10}$$

Ideally, adaptive beamforming should make $\boldsymbol{a}_B\left(\theta, \varphi_f\right)$ independent of the real-time yaw angle, i.e.,

$$\boldsymbol{a}_B(\theta) = \boldsymbol{a}_B\left(\theta, \varphi_f\right). \tag{11}$$

Adaptive beamforming is performed to compensate for yaw rotation by making the real-time beams identical to the reference beams, which are fixed to the ground. Therefore, the steering vector in the beam domain is unvaried, while the steering vector in the antenna domain varies as the platform rotates.

Previously, the GPFB method was developed by restricting the beam shape from rotation when the platform rotated [13]. The solution for this weight vector satisfies the following constraint:

$$\boldsymbol{w}_k\left(\varphi_f\right)\text{s.t.}min\left(\frac{1}{2\pi}\int_0^{2\pi}\int\left|\frac{b_k(\theta,\varphi_\text{f})-\text{b}_{0k}(\theta,\varphi_{\text{f0}})}{\text{K}}\right|^2 d\theta\right) \tag{12}$$

where $b_k\left(\theta,\varphi_f\right)$ represents the real-time adaptive beam, $\text{b}_{0k}(\theta)$ indicates the reference beam, k ($1 \le k \le \text{K}$) denotes the k-th beam channel, and φ_{f0} refers to the reference yaw angle. More specifically, the $b_k\left(\theta,\varphi_f\right)$ and $\text{b}_{0k}(\theta)$ are calculated as follows:

$$b_k\left(\theta,\varphi_f\right)=\boldsymbol{w}_k^{\text{H}}\left(\varphi_f\right)\boldsymbol{a}\left(\theta,\varphi_f\right) \tag{13}$$

$$\text{b}_{0k}(\theta,\varphi_{\text{f0}})=\mathbf{w}_{0k}^{\text{H}}\left(\varphi_f\right)\boldsymbol{a}(\theta,\varphi_{\text{f0}}) \tag{14}$$

where $\boldsymbol{w}_k(\varphi_\text{f})$ is the real-time optimal weight vector while $\mathbf{w}_{0k}$ is the reference weight vector. This constraint is solved to obtain the weight vector of GPFB, shown as:

$$\boldsymbol{w}_{\text{G}k}\left(\varphi_f\right)=\boldsymbol{R}_\text{G}^{-1}\left(\varphi_f\right)\boldsymbol{r}_\text{G}\left(\varphi_f\right) \tag{15}$$

with

$$\boldsymbol{R}_\text{G}\left(\varphi_f\right)=\frac{1}{2\pi}\int_0^{2\pi}\frac{\boldsymbol{a}\left(\theta,\varphi_f\right)\boldsymbol{a}^{\text{H}}\left(\theta,\varphi_f\right)}{\text{K}^2}d\theta$$

$$\boldsymbol{r}_{\text{G}k}\left(\varphi_f\right)=\frac{1}{2\pi}\int_0^{2\pi}\frac{\boldsymbol{a}\left(\theta,\varphi_f\right)\text{b}_{0k}^{\text{H}}(\theta,\varphi_{\text{f0}})}{\text{K}^2}d\theta$$

where $(\cdot)^{-1}$ denotes the inverse of a matrix.

In addition, it was found that GPFB may cause SNR loss when considering the measured antenna distortions, which is attributed to the failure in constraining the norm of $\boldsymbol{w}_{\text{G}k}\left(\varphi_f\right)$, thus leading to a rise in noise after adaptive beamforming [21]. To address this problem, BGPFB is further proposed with constraints imposed on the norm of the weight vector. The new constraints of BGPFB are expressed as:

$$\boldsymbol{w}_k\left(\varphi_f\right)\ s.t.\begin{cases}min\left(\frac{1}{2\pi}\int_0^{2\pi}\int\left|\frac{b_k(\theta,\varphi_\text{f})-\text{b}_{0k}(\theta,\varphi_{\text{f0}})}{\text{K}}\right|^2 d\theta\right)\\ \frac{\left\|\boldsymbol{w}_\text{k}\left(\varphi_f\right)\right\|^2}{\left\|\mathbf{w}_{0\text{k}}\right\|^2}<1\end{cases} \tag{16}$$

On the one hand, it is necessary to make the real-time beam shape as similar to the reference beam as possible. Therefore, the factor called the beam shape keeping factor (BSKF) can be defined as:

$$\text{BSKF}_k\left(\boldsymbol{w}_k\left(\varphi_f\right)\right)=\frac{1}{2\pi}\int_0^{2\pi}\left|\frac{b_k(\theta,\varphi_\text{f})-\text{b}_{0k}(\theta,\varphi_{\text{f0}})}{\text{K}}\right|^2 d\theta. \tag{17}$$

On the other hand, to prevent the SNR loss caused by GPFB, the norm-2 of $\boldsymbol{w}_k\left(\varphi_f\right)$ must be restricted as well. The factor called gain of noise power (GNP) can be defined as:

$$\text{GNP}_k\left(\boldsymbol{w}_k\left(\varphi_f\right)\right)=\frac{\boldsymbol{w}_k^{\text{H}}\left(\varphi_f\right)\boldsymbol{w}_k\left(\varphi_f\right)}{\mathbf{w}_{0k}^{\text{H}}\mathbf{w}_{0k}}. \tag{18}$$

To solve the constraint in (16), one balance factor ξ is introduced to balance the contribution of the two constraint equations, which is a non-negative real number. Therefore, the two constraint equations can be defined in one equation as:

$$\mathrm{B}\left(\boldsymbol{w}_k\left(\varphi_f\right)\right) = \mathrm{BSKF}_k\left(\boldsymbol{w}_k\left(\varphi_f\right)\right) + \xi \mathrm{GNP}_k(\boldsymbol{w}_k\left(\varphi_f\right)). \tag{19}$$

Thus, the constraint Equation (16) can be expressed as:

$$\boldsymbol{w}_k\left(\varphi_f\right) \mathrm{s.t.} \begin{cases} min\left(\mathrm{B}\left(\boldsymbol{w}_k\left(\varphi_f\right)\right)\right) \\ \mathrm{GNP}_k\left(\boldsymbol{w}_k\left(\varphi_f\right)\right) < 1 \end{cases} \tag{20}$$

This solution of BGPFB can be obtained as:

$$\boldsymbol{w}_{\mathrm{BG}k}\left(\varphi_f\right) = \left[\boldsymbol{R}_G\left(\varphi_f\right) + \frac{\xi}{\mathbf{w}_{0k}^{\mathrm{H}}\mathbf{w}_{0k}}\mathbf{I}\right]^{-1} \boldsymbol{r}_{\mathrm{G}k}\left(\varphi_f\right). \tag{21}$$

This method is applicable to avoid the loss of SNR by choosing one suitable balance factor that makes ${\boldsymbol{w}_k}^{\mathrm{H}}\left(\varphi_f\right)\boldsymbol{w}_k\left(\varphi_f\right)$ less than ${\mathbf{w}_{0k}}^{\mathrm{H}}\mathbf{w}_{0k}$.

Both GPFB and BGPFB can effectively compensate for yaw rotation and reduce the bias of DOA estimation [13,21]. However, the occurrence of antenna pattern distortions poses a challenge in making $\boldsymbol{a}_B\left(\theta, \varphi_f\right)$ independent of the real-time φ_f, i.e., yaw compensation is not ideal. In addition, although BGPFB can avoid the loss of the SNR caused by GPFB, BGPFB should compromise the ability of beam shape control, and hence, the deviation of DOA estimation is higher than that of GPFB [21]. The simulated root mean square bias (RMSB) of the targets in different directions shows that compared to the uncompensated value of 11.9°, BGPFB can reduce the value to 4.2°, but the remaining RMSB is still large. However, BGPFB can reduce the deviation of the uncompensated DOA estimation from 7.8° to 0.7° for a simulated target in the east in the previous work, the performance of the root mean square error (RMSE) and standard deviation (SD) of the target in this direction is still acceptable. However, for the DOA estimation of simulation targets in other directions, the estimation deviation of BGPFB may be as high as more than ten degrees. The balanced-focusing pseudo-fixed beamforming (BFPFB) proposed in this paper is used to further eliminate these uncompensated DOA estimation biases. It reduces the constraint range of the azimuth, involving two parameters: the focusing center θ_c and the focusing length θ_l. Then, the two parameters are determined under an iterative strategy. The BFPFB and the iterative strategy are detailed as follows.

2.3. Iterative Adaptive Beamforming

2.3.1. Balanced-Focusing Pseudo-Fixed Beamforming

To enhance the ability of beam shape control, the constraint range of the azimuth is reduced and a modified adaptive beamforming is obtained. This focusing concept of adaptive beamforming is displayed in Figure 3, where the focusing center θ_c and focusing length θ_l are used to define the reduced constraint azimuth range. The red solid line denotes the beam shape in the focusing range after adaptive beamforming. The optimal weight vector is supposed to satisfy (22), the integral interval of which is the main change relative to the constraint equation in (16). In the previous study [21], one conclusion is made that the smaller the BSKF is, the smaller the DOA estimation bias tends to be. BFPFB essentially improves the control of BSKF by reducing the integration range of this metric

and ultimately obtains a smaller BSKF within the focusing range, which can further reduce the DOA estimation bias in comparison with the BGPFB method.

$$\boldsymbol{w}_k\left(\varphi_f\right) \text{s.t.} \begin{cases} min\left(\frac{1}{\theta_l}\int_{\theta_c-0.5\theta_l}^{\theta_c+0.5\theta_l}\left|\frac{b_k(\theta,\varphi_f)-b_{0k}(\theta,\varphi_{f0})}{K}\right|^2 d\theta\right) \\ \left\|\boldsymbol{w}_k\left(\varphi_f\right)\right\|^2/\|\mathbf{w}_{0k}\|^2 < 1 \end{cases} \tag{22}$$

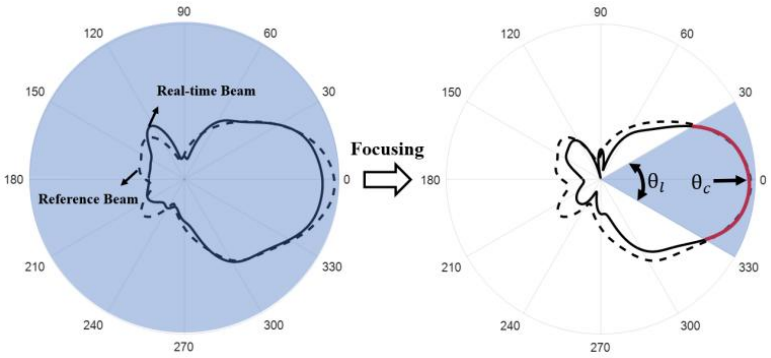

Figure 3. The focusing idea for adaptive beamforming.

The weight vector of BFPFB is obtained as:

$$\boldsymbol{w}_{\mathrm{BF}k}\left(\varphi_f\right) = \left[\boldsymbol{R}_F\left(\varphi_f\right) + \frac{\xi}{\mathbf{w}_{0k}^{\mathrm{H}}\mathbf{w}_{0k}}\mathbf{I}\right]^{-1}\boldsymbol{r}_{Fk}\left(\varphi_f\right) \tag{23}$$

with

$$\boldsymbol{R}_F\left(\varphi_f\right) = \frac{1}{\theta_l}\int_{\theta_c-0.5\theta_l}^{\theta_c+0.5\theta_l}\frac{\boldsymbol{a}\left(\theta,\varphi_f\right)\boldsymbol{a}^{\mathrm{H}}\left(\theta,\varphi_f\right)}{K^2}d\theta$$

$$\boldsymbol{r}_{Fk}\left(\varphi_f\right) = \frac{1}{\theta_l}\int_{\theta_c-0.5\theta_l}^{\theta_c+0.5\theta_l}\frac{\boldsymbol{a}\left(\theta,\varphi_f\right)b_{0k}^{\mathrm{H}}(\theta,\varphi_{f0})}{K^2}d\theta$$

When the focusing length is set to 2π, the modified adaptive beamforming is simplified to the previous BGPFB. Furthermore, when the balance factor equals zero, the modified adaptive beamforming is just GPFB. Therefore, the adaptive beamforming method based on the focusing concept is regarded as a more general adaptive beamforming scheme.

The primary objective of yaw compensation is to achieve a precise DOA estimation. Figure 4 shows the flowchart of the DOA estimation with BFPFB. For every transmit period, it is necessary to convert radar data from the antenna domain into the beam domain at first through adaptive beamforming. Then, more precise DOA estimation results can be obtained by using the direction-finding methods in the beam domain. It is noteworthy that the determined balance factor ξ_D is the balance factor that makes the $\left\|\boldsymbol{w}_{\mathrm{BF}k}\left(\varphi_f\right)\right\|^2$ less than $\|\mathbf{w}_{0k}\|^2$ and reduces the integral errors between $b_k\left(\theta,\varphi_f\right)$ and $b_{0k}(\theta)$ as much as possible. In this paper, it is proved that the BSKF monotonically increases as the balance factor increases (Appendix A), and the GNP monotonically decreases as the balance factor increases (Appendix B). Then, the balance factor can be obtained by making GNP equal to zero decibels through the Bisection method, thus reducing computational time significantly.

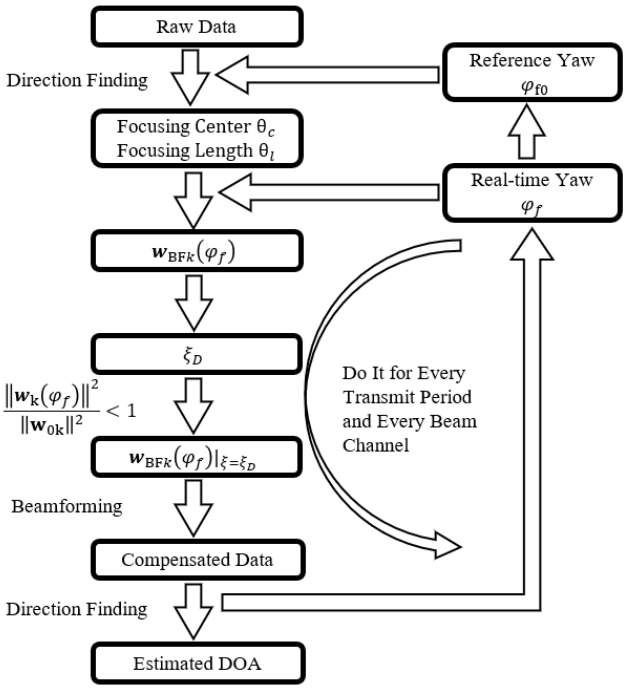

Figure 4. Flowchart of DOA estimation through BFPFB.

2.3.2. Iterative Determination of Focusing Center and Focusing Length

To realize BFPFB, two key parameters should be predetermined: the focusing center θ_c and the focusing length θ_l. This means determining the constraint range of the azimuth $[\theta_c - 0.5\theta_l, \theta_c + 0.5\theta_l]$, which can also be called the focusing range.

It is expected that the focusing center is as close to the true direction as possible and that the focusing length is as short as possible. However, there are two contradictions: (1) BFPFB aims mainly for precise DOA estimation results, but the use of this algorithm also involves precise DOA estimation results as the focusing center; (2) a shorter focusing length is required for more effective control of the beam shape, but a shorter focusing length is more likely to cause the true DOA to fall outside the focusing range. Given the two contradictions, one iterative determination strategy of the focusing range is proposed here.

From the last iteration to the current iteration, the focusing center of the current iteration can be set as the estimated DOA of the last iteration, and the current focusing length is supposed to be shorter than the last focusing length. A reasonable solution to reducing the focusing length is proportional reduction. The relationship of the focusing length between the current iteration and the last iteration is expressed as:

$$\theta_{l_current} = \theta_{l_last} / \mathrm{R_L} \tag{24}$$

where $\mathrm{R_L}$ is the reduction rate of the focusing length. When $\mathrm{R_L}$ is large, the iteration speed is high, but the true DOA is more likely to fall outside the focusing range. Conversely, when $\mathrm{R_L}$ is small, the iteration speed is slow, but the true DOA is more likely to fall within the focusing range. Therefore, one suitable reduction rate of the focusing length should be chosen for the use of iterative BFPFB.

2.4. DOA Estimation with Iterative BFPFB

The flowchart of the DOA estimation using iterative BFPFB is shown in Table 1. The iteration is from step 2 to step 4, which should be conducted more than once. θ_o represents the current result of DOA estimation, and θ_{lT} refers to the threshold of the focusing length

that decides when the iteration is over. Notably, the focusing center can be set as any direction in the initialization because the initial focusing length is 2π.

Table 1. Flowchart of DOA estimation using iterative BFPFB.

Algorithm: DOA Estimation Using Iterative BFPFB	
1	Initialization: $\theta_c = 0°$, $\theta_l = 360°$, $R_L = 2$;
2	DOA estimation using BFPFB: θ_o;
3	Updation: $\theta_c = \theta_o$, $\theta_l = \theta_l / R_L$;
4	Iteration Decision: if $\theta_l < \theta_{lT}$, go to step 5; else, go to step 2;
5	Output: θ_o.

3. Simulation

One iterative adaptive beamforming of the focusing concept has been described above to improve the yaw compensation performance. In this section, the simulation settings are first introduced, especially the antenna distortions measured in a field experiment. Then, an analysis is conducted on the yaw compensation performance for DOA estimation.

3.1. Simulation Settings

The simulation settings remain the same as those in [13,21]. The operating frequency is 13.15 MHz, and the receive array is one eight-element circular array with a radius of 6 m. One half-sine rotation (HSR) is taken as the yaw rotation that can be defined in (25), where the yaw range Y_s is 90° and the CIT denoted as T_a is 300 s. To iteratively determine the focusing range, R_L is set as 2, and θ_{lT} is set as $\pi/8$.

$$\varphi_{\mathrm{HSR}}(t) = -\frac{Y_s}{2} + Y_s \sin\left(\frac{\pi}{T_a} t\right), 0 \le t \le T_a \tag{25}$$

Notably, antenna distortions are inevitable for a high-frequency array on a floating platform because of space limits [22]. Figure 5 shows the measured antenna distortions for an eight-element circular array with a radius of 6 m. This array and the antenna distortions are used for the subsequent simulations. The amplitude distortions fluctuate between −2.5 dB and +2.5 dB, while the phase distortions fluctuate between −40° and +40°. According to previous DOA estimation results, the antenna distortions can cause deterioration in the yaw compensation performance of both GPFB [13] and BGPFB [21]. This newly proposed iterative adaptive beamforming aims mainly to improve the DOA estimation performance when the measured antenna distortions are taken into account.

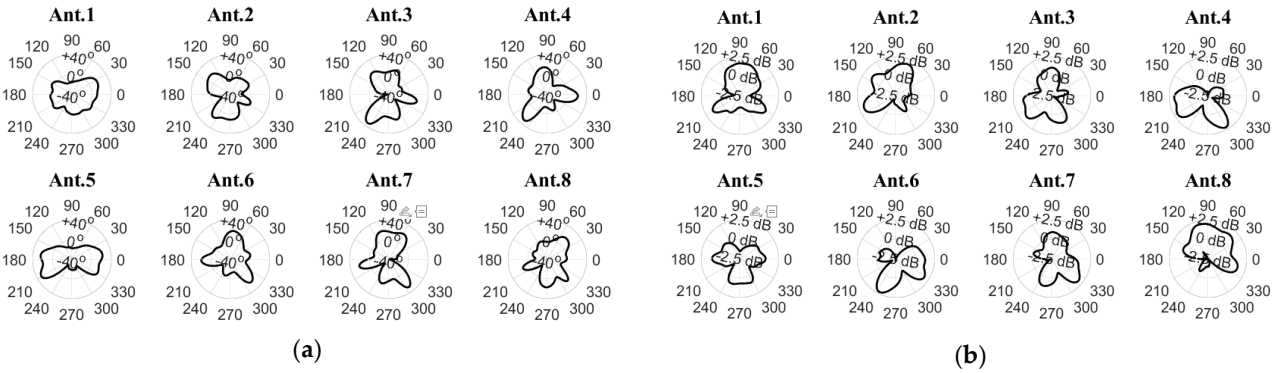

Figure 5. Antenna distortions: (**a**) phase distortions; (**b**) amplitude distortions.

3.2. DOA Estimation Results for Simulation Object

3.2.1. MUSIC Spectrum

Due to the limited array aperture, MUSIC has been widely applied to the DOA estimation for HFSWR [23,24]. Considering one far-field object from the southeast, the MUSIC spectra for different focusing lengths are shown in Figure 6. The search step for the MUSIC spectrum is 0.1°, which is used in the simulations and the following field experiments. Noise is not introduced in this case to consider only the influence of signal modulation on the azimuth spectrum. As the focusing length decreases, the DOA biases are 10.6°, 6.4°, 2.1°, 0.5°, 0.1°, and 0.0°, respectively. A shorter focusing length tends to result in a smaller DOA bias, which indicates that the BFPFB with a short constraint range is effective in minimizing the DOA estimation bias. Furthermore, the search spectrum becomes sharper as the focusing length decreases. This is because the stability of the steering vector in the beam domain is improved as the focusing length decreases. It is also implied that the proposed algorithm may be more suitable than the DBF-based compensation method for the DOA estimation of multiple objects whose arrival angles are close to each other.

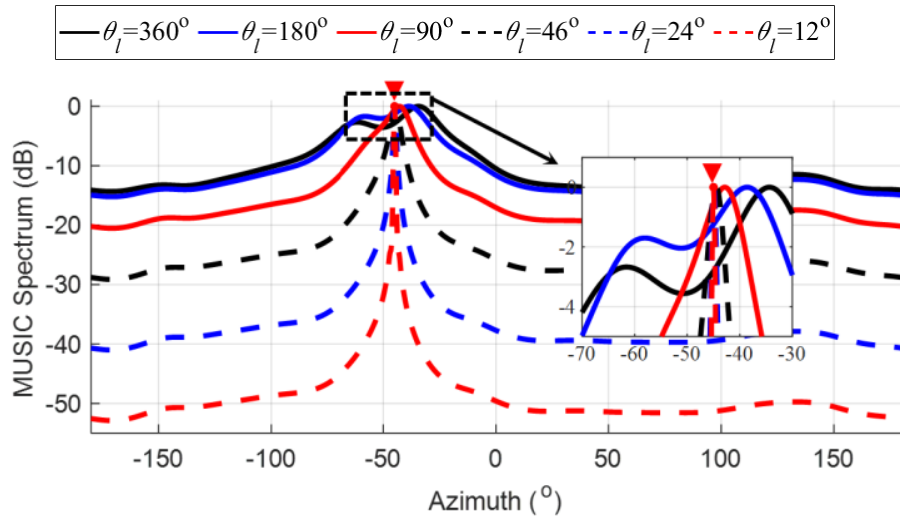

Figure 6. MUSIC spectra of one simulation object from the southeast for different focusing lengths. The true direction is denoted as a red downward triangle.

To better understand how the BFPFB affects the two parameters, GNP and BSKF, and thus reduces the bias of the DOA estimation, for the southeast target simulated in the paper, the corresponding characteristic curves of GNP and BSKF varying with the balance factor are shown in Figure 7. We assume that the real-time yaw angle is 100° and the reference yaw angle is 0°. The black circles in the figure indicate the decided GNP and BSKF of GPFB, and the red circles indicate the corresponding values of BFPFB. It should be noted that the characteristic curve of BFPFB is just the BGPFB characteristic curve when the focusing length is 360°. Firstly, the relationship of the two parameters between GPFB and BGPFB is analyzed. Since GPFB only constrains the BSKF but not the GNP, the GNP and BSKF of GPFB are just the corresponding values on the characteristic curves of BGPFB when the balance factor is equal to zero. Moreover, since the characteristic curves of BGPFB converge to the GNP and BSKF of GPFB when the balance factor decreases. In such a case, when the balance factor is less than −30 dB, the two characteristic curves have converged. Therefore, the GNP and BSKF of GPFB can be decided as the values on the characteristic curves of BGPFB when the balance factor takes the minimum value in the range of the displayed balance factor. The GNP of GPFB is 10.4 dB, then according to the conclusion obtained in the previous study [21], it can be seen that the GPFB will bring about an SNR

loss of 10.4 dB. Since the GNP monotonically decreases with the balance factor which is proved in Appendix B, and the previous study pointed out that the minimum value of GNP is zero [21], increasing the balance factor will certainly make the GNP less than 0 dB. Then, according to Appendix A, since the BSKF monotonically increases with the balance factor, the DOA estimation requires a small BSKF to ensure that the estimation bias is as small as possible. Hence, the balance factor should take the value when GNP is equal to 0 dB to avoid SNR loss and make BSKF as small as possible. Correspondingly, the value of BSKF for BGPFB is obtained. This value must be larger than that of GPFB, which also indicates that BGPFB needs to sacrifice the BSKF performance to ensure that the GNP is not larger than zero dB. Then, the relationship of the GNP and BSKF between BGPFB and BFPFB is analyzed. By the same method, when the focusing length decreases, the balance factor when the GNP is equal to zero dB is taken to obtain the corresponding BSKF of BFPFB, which gradually decreases with the decrease in the focusing length and decreases from -17.2 dB for the initial focusing length of 360° to -42.9 dB for the focusing length of 12°. Previous studies have shown that the inverse of BSKF approximates to the signal-to-modulation ratio (SMR) [21]; namely, the SMR rises from an initial 17.2 dB to 42.9 dB. The SMR is similar to the SNR, so as the focusing length decreases, the BSKF of BFPFB decreases, and the DOA estimation bias decreases.

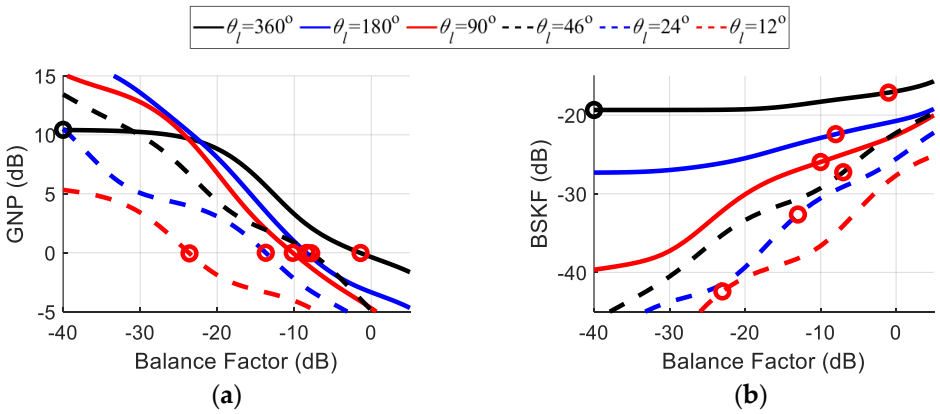

Figure 7. Gain of noise power (GNP) and beam shape keeping factor (BSKF) for different balance factors ($\theta_c = -45°$, $\varphi_f = 100°$, $\varphi_{f0} = 0°$). (**a**) GNP versus balance factor; (**b**) BSKF versus balance factor.

In summary, the newly proposed iterative adaptive beamforming can significantly improve the MUSIC spectrum from two perspectives as the focusing length decreases: (1) the peak bias is reduced, i.e., the DOA bias is smaller; (2) the peak becomes sharper, indicating that the algorithm is applicable to improve the DOA estimation for adjacent objects.

3.2.2. Statistical Results of DOA Estimation

In this part, the DOA estimation performance is analyzed under different SNR conditions. With additive white Gaussian noise introduced, the SNR in every antenna channel is set to range from 10 dB to 30 dB. Figure 8 presents the statistical results obtained through the 2000 Monte-Carlo experiments. One thing should be noted that the bule dashed lines are all very close to the red dashed lines, which means the performances of focusing length of 24° are just the same as those of focusing length of 12°.

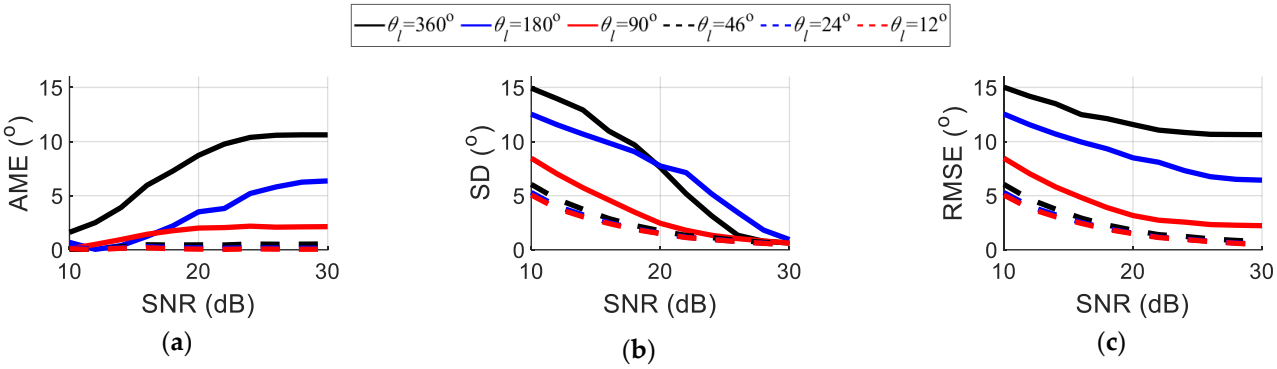

Figure 8. Statistical results of DOA estimation under different focusing lengths: (**a**) absolute mean error (AME); (**b**) standard deviation (SD); (**c**) root mean square error (RMSE).

The absolute mean error (AME) represents the bias of the DOA estimation. As shown in Figure 8a, when the SNR increases, all AMEs converge to the corresponding DOA biases, which are estimated in Figure 6. When the SNR is small, the AME is also smaller, which is a rather strange phenomenon. Further study shows that this phenomenon is related to the structure of the MUSIC search spectra. Taking the BFPFB with a focusing length of 360° as an example, there are two high peaks in the corresponding search spectrum in Figure 6, with peaks of −61.5° and −34.4°, respectively. The two peaks are distributed on both sides of the true value, and the deviations from the true value are −16.5° and 10.6°, respectively. To better understand it, the histogram of the frequency distribution of the DOA errors is further plotted, as shown in Figure 9. When the SNR is 10 dB, due to the low SNR, there are many estimation results near the two high peaks, resulting in the frequency of the DOA errors centering −16.5° and 10.6°, then the AME is close to zero. When the SNR is 30 dB, due to the high SNR, the DOA estimation results are mainly concentrated around the highest peak on the right side. Hence, the frequency of the DOA estimation errors is centered at 10.6°, and the AME is close to the DOA estimation bias of 10.6°. This phenomenon further demonstrates the superiority of the focusing adaptive beamforming with a small focusing length.

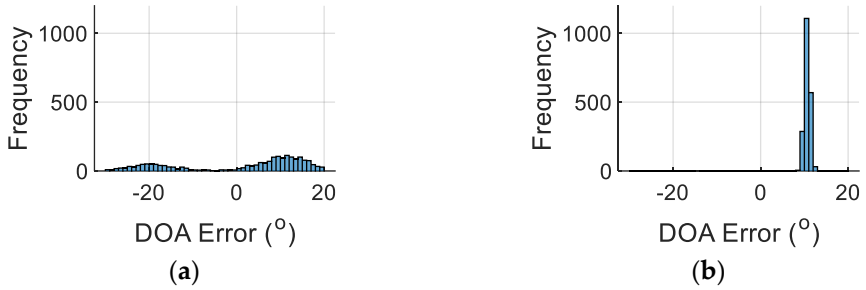

Figure 9. Histogram of the frequency distribution of DOA errors of the simulated target ($\theta_l = 360°$): (**a**) SNR = 10 dB; (**b**) SNR = 30 dB.

SD indicates the stability of the DOA estimation. It is generally believed that this parameter is mainly related to the SNR of the echo. Also, as confirmed by the simulation results, this parameter decreases significantly as the SNR increases. In addition, the SD shows a decreasing trend as the focusing length decreases. One reason may lie in that adaptive beamforming compensates for the Doppler modulation caused by the yaw rotation of the platform, which increases the SNR of echoes. When the focusing length is smaller, the SNR improvement is more significant. Simply analyzing the SNR is inadequate to explain the SD results of Figure 8b with different focusing lengths. Due to the limited loss of the SNR caused by yaw rotation, the difference in SNRs obtained by different focusing

lengths is insignificant, and the difference in SDs with different focusing lengths should not be large either. However, when the focus length is 360 degrees or 180 degrees, the SDs are significantly larger than those in other cases. Hence, another reason may lie in that when the focusing length is larger, the beam control ability of adaptive beamforming is weaker and the spatial spectrum is broadened more seriously. When the focusing length is 360 degrees or 180 degrees, its MUSIC even exhibits two peaks. That is to say, when the SNR is low, there are two distribution centers for its DOA estimation, which is shown in Figure 9a.

RMSE can be used to evaluate both the mean error and the standard deviation comprehensively. Although the RMSE remains large when the focusing length equals 360° in Figure 8c, the improvement in the RMSE is obvious as the focusing length decreases. When the focusing length is less than 46 degrees, the difference in RMSEs is insignificant, and all of them are at a low level. It indicates that an especially small focusing length is not requisite to achieve a better compensation performance, which illustrates the practicality of the method proposed in this paper.

In summary, there are two ways in which yaw rotation can influence the DOA estimation: DOA bias and DOA stability. The proposed BFPFB can improve the beam shape control ability significantly, and more precise and stable DOA estimation results can be obtained through iterative adaptive beamforming with a shorter focusing length.

4. Experimental Results

4.1. Experimental Description

The field experiment discussed here was performed in the Taiwan Strait jointly by China Precise Ocean Detection Technology Co., Ltd. from Yichang, China and the Radio Oceanography Laboratory of Wuhan University in December 2016. The working parameters are all identical to those in the simulation parts. One floating HF radar was anchored in the sea, with two shore-based radars (Radar A and Radar B) working synchronously (see Figure 10). Figure 11 shows the typical range-Doppler spectrum received by the floating radar. The echoes from range bin zero to range bin forty are the backscatter of the signal transmitted by the floating radar. The typical ship backscatter shown in the figure always has an isolated peak. The signals supposed to be emphasized are the cooperative signals from radar A and radar B, which propagate from the transmitting antenna of the shore-based radar directly to the receiving antenna of the floating radar. Consequently, the cooperative signals are much stronger than ship echoes. In the following parts, the results of the cooperative signals and ship echoes will be discussed.

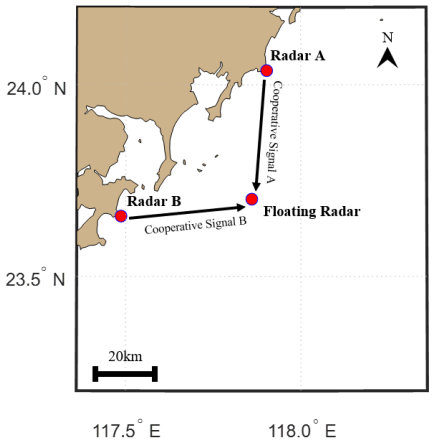

Figure 10. The geographical structure of one radar network consisting of one floating HF radar and two shore-based HF radars.

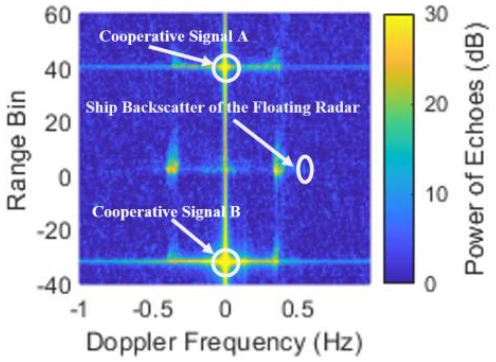

Figure 11. The typical range-Doppler spectrum for the floating radar, with two cooperative signals from two onshore radars.

4.2. Results for Cooperative Signals

The cooperative signals are the direct waves from two shore-based radars, the DOA estimation of which is hardly influenced by interference or background noise. For this reason, the biases of DOA estimation are assessed using the two cooperative signals. Figure 12a presents the true azimuth of the cooperative signal from Radar B. The true azimuth of the cooperative signal is −172.7°, which is calculated from the longitudes and latitudes of the floating radar and Radar B. Figure 12b displays the yaw angle during one case on 26 December 2016 at 09:14:49. The yaw range of this case is 71.4°. Figure 12c shows the Doppler spectrum for the range bin where the cooperative signal is. Evidently, the SNR of this cooperative signal is as large as about 80 dB, as a result of which the influence of noise or interference can be reduced to a minimum. In other words, the cooperative signal is the ideal source suitable for evaluating the DOA bias of the yaw compensation methods.

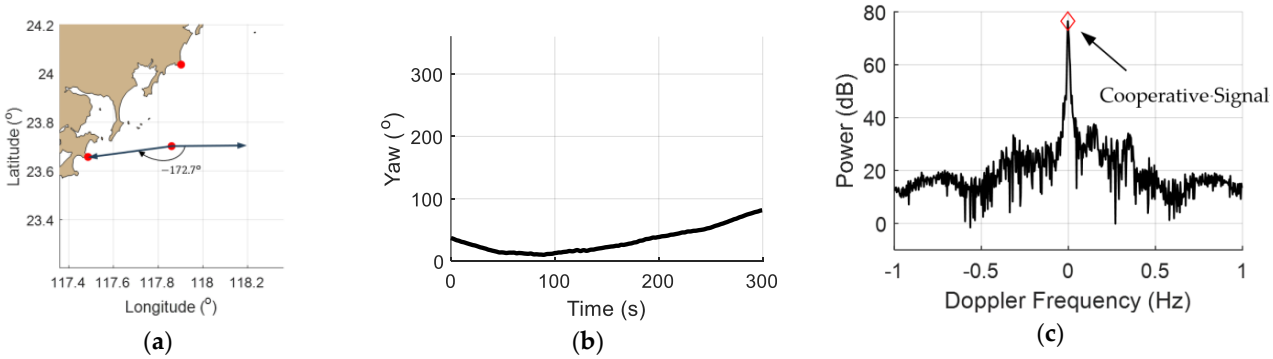

Figure 12. The case of cooperative signal B on 26 December 2016 at 09:14:49: (**a**) the true azimuth for this cooperative signal; (**b**) the yaw angle during this case. (**c**) the Doppler spectrum for the range bin where the cooperative signal is present.

Figure 13 illustrates the MUSIC spectra for this cooperative signal. When the focusing length decreases, the DOA errors are 15.3°, 10.8°, 4.6°, 1.5°, 0.5°, and 0.4°, respectively. The results are comparable to those in the simulation in Figure 6. As the focusing length decreases, the DOA errors are reduced, and the spectra become sharper. However, it should be noted that the DOA error cannot be eliminated, even when the focusing length is as small as 12°. This is because of some other factors that cannot be avoided, such as the error of the yaw angle, the error of antenna distortions, the influence of pitch and roll rotations, etc. However, it is evident that the main influencing factor in the DOA error is yaw rotation rather than the other factors when the SNR is sufficiently high.

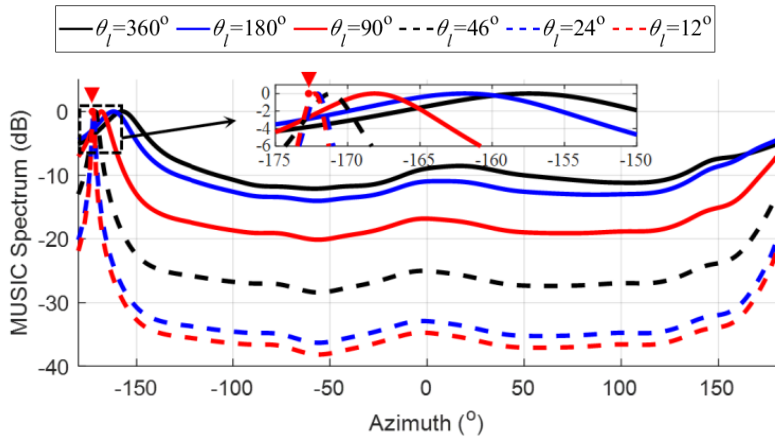

Figure 13. The MUSIC spectra of the cooperative signal in Figure 12. The true direction is denoted as a red downward triangle.

Figure 14 shows the DOA errors against the yaw ranges for all the cases of the two cooperative signals. According to the outcomes documented in previous work for GPFB [13] and BGPFB [21], global adaptive beamforming fails to eliminate the DOA bias due to the antenna distortions, despite its effectiveness in reducing these biases. When the focusing length decreases, the DOA errors are less scattered and closer to zero. Furthermore, Table 2 lists the RMSEs of the DOA estimations over different intervals of the yaw range. For a focusing length of less than 46°, the RMSEs are all smaller than one degree for both two cooperative signals, confirming that the proposed BFPFB is capable of further reducing the errors compared to the global adaptive beamforming method. When the focusing length is equal to 360 degrees, the RMSEs of the two cooperative signals increase significantly as the yaw range increases. In addition, the RMSEs of cooperative signal B are obviously larger than those of cooperative signal A, indicating an obvious orientation difference in the performance of BGPFB. It is demonstrated that the compensation performance of BGPFB deteriorates as the yaw range increases due to its limited ability of beam shape control. When the focusing length is equal to 12 degrees, the RMSEs of the two cooperative signals are irrelevant to the yaw range, suggesting that the method proposed in this paper produces an excellent compensation performance when the focusing length is small. Furthermore, when the focusing length decreases from 24 degrees to 12 degrees, there is no obvious decline in the RMSEs of the two cooperative signals, which also indicates that the influence of other systematic errors causes the focusing length equal to 24 degrees to reach the limit of such a floating HFSWR.

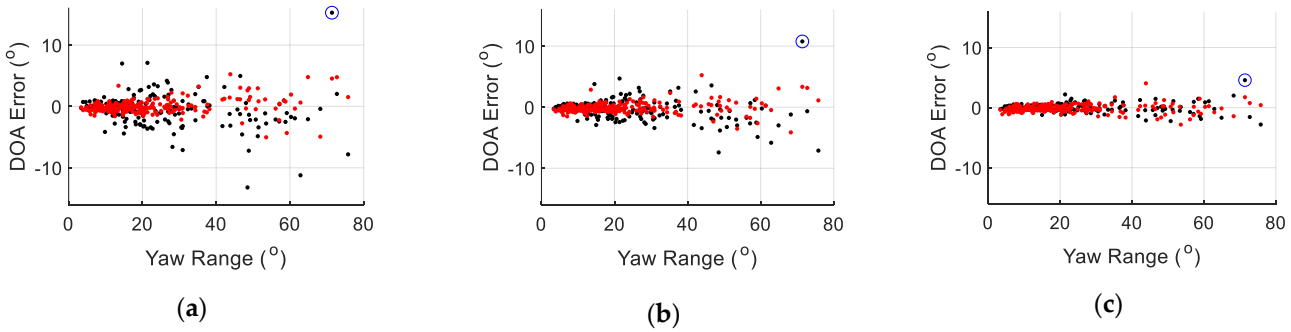

Figure 14. *Cont.*

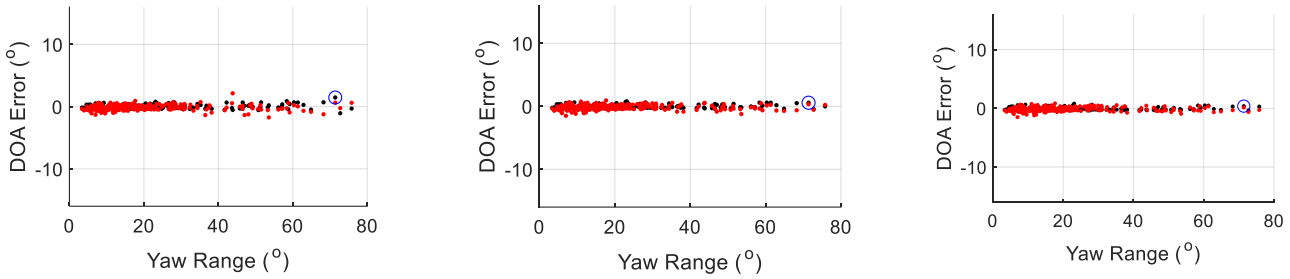

Figure 14. The DOA errors of the two cooperative signals with yaw range. The red points represent the results of cooperative signal A, while the black points represent the results of cooperative signal B. The result in the blue circle is the case in Figures 12 and 13: (**a**) $\theta_l = 360°$; (**b**) $\theta_l = 180°$; (**c**) $\theta_l = 90°$; (**d**) $\theta_l = 46°$; (**e**) $\theta_l = 24°$; (**f**) $\theta_l = 12°$.

Table 2. The DOA RMSEs of two cooperative signals over different intervals of yaw range.

Cooperative Signal	Focusing Length	[0°,10°) [a] (47) [b]	[10°,20°) (87)	[20°,30°) (44)	[30°,40°) (17)	[40°,100°) (32)
A	360°	0.6°	0.7°	0.9°	1.3°	2.7°
	180°	0.5°	0.6°	0.7°	1.0°	1.9°
	90°	0.5°	0.4°	0.5°	0.9°	1.3°
	46°	0.5°	0.4°	0.4°	0.5°	0.7°
	24°	0.5°	0.4°	0.3°	0.4°	0.5°
	12°	0.5°	0.4°	0.3°	0.4°	0.4°
B	360°	0.7°	1.5°	2.7°	2.8°	5.0°
	180°	0.4°	0.9°	1.7°	1.7°	3.5°
	90°	0.2°	0.3°	0.7°	0.6°	1.5°
	46°	0.2°	0.2°	0.3°	0.2°	0.5°
	24°	0.2°	0.2°	0.3°	0.2°	0.3°
	12°	0.2°	0.2°	0.3°	0.2°	0.3°

[a] The square bracket on the left indicates that the yaw range is greater than or equal to the corresponding value, and the round bracket on the right indicates that the yaw range is less than the corresponding value. [b] The number in the bracket is the sample number.

4.3. Results for Ships

Ship detection is a crucial function of floating HF radar. Herein, the case of one typical ship echo is discussed. Figure 15 shows the true azimuth, the yaw angle, and the corresponding Doppler spectrum. The yaw range, in this case, is 34.3°. The true azimuth of the ship is −156.0°. The SNR of ship echoes is around 15 dB, which is considerably smaller than those of cooperative signals.

The MUSIC spectra of this ship are displayed in Figure 16. When the focusing length decreases, the DOA errors are −17.8°, −11.7°, −9.6°, −2.9°, −1.0°, and −1.0°, respectively. In general, the DOA errors decrease when the focusing length decreases. However, the phenomenon that the spectra become sharper as the focusing length decreases is not as obvious as those in Figure 13. This is because the SNR of the ship echoes is much smaller than that of the cooperative signal. This also explains why the DOA errors remain high or even fluctuate significantly as focusing length decreases (see Table 3). For the ship echoes of floating HF radar, the DOA error of ships can be affected by both the SNR and platform yaw rotation. The proposed method is applicable to minimize the negative impact of yaw rotation.

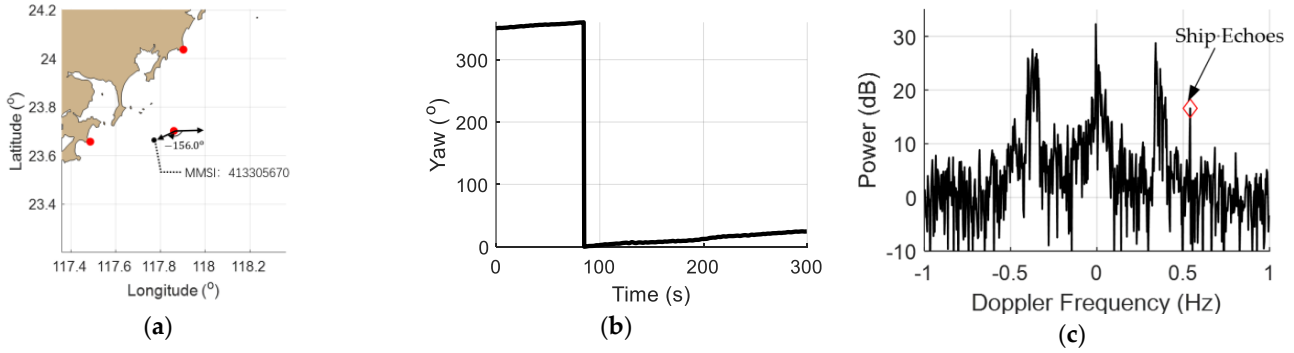

Figure 15. The case of the typical ship echoes. The maritime mobile service identity (MMSI) of this ship is 413305670: (**a**) the true azimuth of this ship; (**b**) the yaw angle during this case; (**c**) the Doppler spectrum for the range bin where the ship echoes are present.

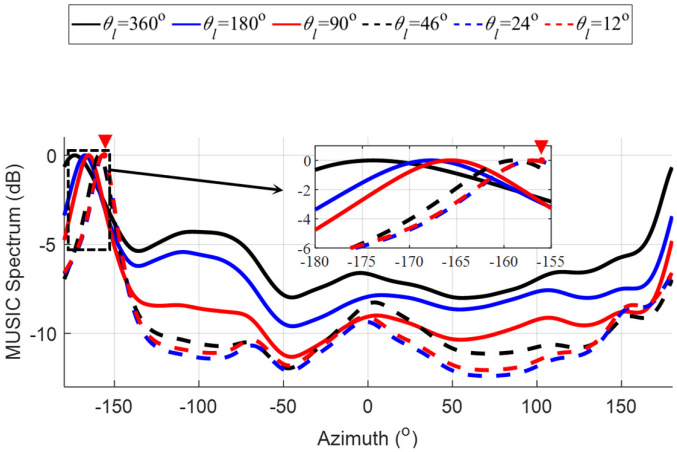

Figure 16. The MUSIC spectra of the typical ship echo. The true direction is denoted as a red downward triangle.

Table 3. DOA errors after iterative adaptive beamforming.

Focusing Length	360°	180°	90°	46°	24°	12°
09:04:49 (153.7°) [a]	−5.0°	−4.8°	−4.9°	−4.1°	−4.4°	−4.0°
09:09:49 (−154.7°)	−1.5°	−0.7°	−2.4°	−1.8°	−1.8°	−1.4°
09:14:49 (−156.0°)	**−17.8°**	**−11.7°**	**−9.6°**	**−2.9°**	**−1.0°**	**−1.0°**
09:19:49 (−158.1°)	3.1°	2.8°	2.7°	2.6°	2.5°	2.0°

[a] The angle in the bracket is the current true azimuth.

5. Discussion

In this paper, we first constructed a signal model of the floating HFSWR and focused on analyzing the steering vector that affects the DOA estimation. To compensate for the changes in the steering vector due to the platform rotations in one CIT, a rotation compensation scheme based on adaptive beamforming was introduced, i.e., the steering vector in the antenna domain was converted to the steering vector in the beam domain by beamforming, and the steering vector in the beam domain was made to remain constant when the platform rotates. However, due to the influence of the actual antenna distortions, the ability of beam shape control of the global adaptive beamforming methods, GPFB and BGPFB, is limited, which does not ensure the beam is completely unchanged. For this reason, based on the concept of focusing, the angular constraint range of beamforming was narrowed to improve the beamforming capability in the focusing range.

The improvement in DOA estimation by focusing on adaptive beamforming is mainly in the aspects of stability and accuracy. In terms of the stability of DOA estimation, the steering vector of the global adaptive beam still changes during the rotation due to the limited beam control capability, which ultimately manifests itself as a broadening of the beam-domain spatial spectrum, which leads to a lower stability of DOA estimation. After focusing, the steering vectors in the beam domain are much more aggregated, and there is almost no broadening of the spatial spectrum in the beam domain, and the stability of the DOA estimation is significantly improved. It is worth noting that the stability of the DOA estimation for different focusing lengths exhibits great differences when the SNR is low. When the focusing length is large, the azimuthal search spectrum may have multiple peaks, at which time the stability of the DOA estimation may be low. When the focusing length is small, the azimuthal search spectrum only has one obvious peak; hence, the stability of the DOA estimation is good. In terms of the accuracy of DOA estimation, also due to the limited beamforming capability of the global adaptive beamforming, the real-time beam-domain steering vectors have an uncertain deviation from the reference steering vectors, which is ultimately manifested as DOA estimation bias. The steering vector formed by the focusing beamforming has a much smaller deviation from the reference steering vector in the focusing range, and hence, the DOA estimation bias can be eliminated. Although the BFPFB proposed in this paper shows much better DOA estimation performance than the global adaptive beamforming, some aspects still need to be further considered in the process of using it.

First, only the compensation of the yaw angle was considered, while the pitch and roll angles of platform rotation were ignored in this paper. This is due to the fact that the pitch and roll angles are small in low-sea state scenarios. If the floating HFSWR operates in high-sea state scenarios, the effects of pitch and roll on DOA estimation need to be considered.

Secondly, since HFSWR first receives the range-Doppler spectrum before the angle estimation, the general vessel target is just an isolated point on this two-dimensional spectrum, and this paper is only aimed at this single target application scenario. If the target falls within the first-order sea backscatter, then the multi-target application scenario should be considered. Although the newly proposed method can improve the stability and accuracy of the DOA estimation of a single target, this focusing adaptive beamforming, which is mainly characterized by a focusing center and focusing length, cannot effectively deal with the multi-targets in different directions and needs to be further explored.

Thirdly, the computation time needed for each iteration of BFPFB is just the time consumption of BGPFB. Since the method proposed in this paper needs to be realized iteratively, the time consumption of BFPFB is the time consumption of BGPFB multiplied by the number of iterations. How to reduce the time consumption of BFPFB is a problem to be considered in the process of practical application. Evaluating the range of the DOA error of BGPFB first should be considered, according to which the focusing length is directly reduced from 360° to a much smaller focusing length so that the number of iterations can be reduced.

Finally, while this paper improves the stability of DOA estimation through beam-domain steering vector improvement, it ignores the effect of the SNR loss caused by translations. In low-sea state scenarios, the effect of SNR loss due to translations can be ignored. However, in high-sea state scenarios, the translations of the floating platform are more intense, and the SNR loss cannot be ignored. This paper aims to compensate for yaw rotation and further improve the performance of DOA estimation. Future work scenarios would include synergies with anti-jamming signal design [25] to enhance robustness against adversarial interference while incorporating advanced target detection frameworks such

as azimuth trajectory modeling [26] and sub-band feature fusion [27] for multi-modal maritime surveillance.

6. Conclusions

In this paper, an iterative adaptive beamforming of the focusing concept is proposed to improve the yaw compensation performance when the measured antenna distortions are taken into account. Firstly, one adaptive beamforming, called BFPFB, is proposed by shortening the constraint range of the azimuth. Subsequently, the two key parameters of BFPFB, the focusing center, and the focusing length, are determined through an iterative strategy. Compared with the global adaptive beamforming algorithms, GPFB and BGPFB, the main difference in the focusing adaptive beamforming proposed in this paper is that the adaptive beamforming is performed only in the focusing range. Its advantage is that it can avoid the loss of the SNR caused by GPFB and further reduce or even eliminate the DOA estimation bias of BGPFB. The simulation results indicate that the proposed method can improve the precision and stability of DOA estimation significantly. The BFPFB proposed in this paper can also significantly reduce the DOA errors for two cooperative signals. Moreover, as confirmed by the ship experiment, the iterative BFPFB can minimize the negative effect of yaw rotation on DOA estimation.

However, there are still three areas where further investigation is required: First, although yaw rotation is the main factor affecting the DOA estimation of far-field objects among the 3-DOF rotations, pitch and roll rotations can affect the DOA estimation as well, so our future work will focus on a comprehensive iterative adaptive beamforming with all 3-DOF rotations considered. Second, the yaw compensation performance is analyzed for a single object only. The analysis of multiple objects is another focus of future work. Finally, this paper only focuses on the rotational goniometric problem but neglects the effect of the Doppler modulation of the platform's translations on the SNR loss. Efforts are needed to develop the methods and theories of random translation compensation for a floating platform.

Author Contributions: Conceptualization, X.Y.; methodology, X.Y.; software, X.W. and X.Y.; validation, X.Y.; formal analysis, X.Y; investigation, X.W. and X.Y.; resources, X.W.; data curation, L.Y.; writing—original draft preparation, X.Y.; writing—review and editing, X.Y., M.Q., Z.L. and S.S.; visualization, L.W.; supervision, L.W.; project administration, X.W.; funding acquisition, L.W. All authors have read and agreed to the published version of the manuscript.

Funding: This work was supported in part by the National Natural Science Foundation of China (No. 42306211), the Fund of National University of Defense Technology (No. 23-ZZCX-JDZ-45), and the Key R&D Program of Hubei Province (No. 2020BCA080).

Data Availability Statement: Data cannot be shared because of intellectual property rights.

Acknowledgments: Our gratitude is extended to Wu Xiongbin's Lab at Wuhan University for providing the experimental data.

Conflicts of Interest: The authors declare no conflicts of interest.

Abbreviations

HFSWR	High-frequency surface wave radar
DOF	Degree-of-freedom
CIT	Coherent integration time
DOA	Direction-of-arrival
DBF	Digital beamforming
MUSIC	Multiple signal classification

GPFB	Global pseudo-fixed beamforming
BGPFB	Balanced global pseudo-fixed beamforming
BFPFB	Balanced-focusing pseudo-fixed beamforming
SNR	Signal-to-noise ratio
SMR	Signal-to-modulation ratio
AME	Absolute mean error
SD	Standard deviation
RMSE	Root mean square error
RMSB	Root mean square bias

Appendix A

The monotonicity of BSKF with respect to balance factor ξ is proved as follows:

Substitute the solution of $\boldsymbol{w}_{\mathrm{BF}k}\left(\varphi_f\right)$ in (23) into the definition of BSKF in (17) and the BSKF with respect to the balance factor can be obtained as:

$$\begin{aligned} h(\xi) = \frac{1}{\mathrm{K}^2\theta_l} \int_{\theta_c-0.5\theta_l}^{\theta_c+0.5\theta_l} & \left(\boldsymbol{w}_{\mathrm{BF}k}^{\mathrm{H}}\left(\varphi_f\right)\boldsymbol{a}\left(\theta,\varphi_f\right) - \mathrm{b}_{0k}(\theta,\varphi_{\mathrm{f0}})\right) \\ & \cdot\left(\boldsymbol{w}_{\mathrm{BF}k}^{\mathrm{H}}\left(\varphi_f\right)\boldsymbol{a}\left(\theta,\varphi_f\right) - \mathrm{b}_{0k}(\theta,\varphi_{\mathrm{f0}})\right)^{\mathrm{H}} d\theta. \end{aligned} \tag{A1}$$

Then,

$$h(\xi) = \boldsymbol{w}_{\mathrm{BF}k}^{\mathrm{H}}\left(\varphi_f\right)\boldsymbol{R}_F\left(\varphi_f\right)\boldsymbol{w}_{\mathrm{BF}k}\left(\varphi_f\right) - \boldsymbol{r}_{Fk}^{\mathrm{H}}\left(\varphi_f\right)\boldsymbol{w}_{\mathrm{BF}k}\left(\varphi_f\right) - \boldsymbol{w}_{\mathrm{BF}k}^{\mathrm{H}}\left(\varphi_f\right)\boldsymbol{r}_{Fk}\left(\varphi_f\right) + \mathrm{B}_{0k} \tag{A2}$$

with

$$\mathrm{B}_{0k} = \frac{1}{\theta_l}\int_{\theta_c-0.5\theta_l}^{\theta_c+0.5\theta_l} \frac{\mathrm{b}_{0k}(\theta,\varphi_{\mathrm{f0}})\mathrm{b}_{0k}^{\mathrm{H}}(\theta,\varphi_{\mathrm{f0}})}{\mathrm{K}^2} d\theta.$$

Calculate the differential of $h(\xi)$ with respect to ξ to obtain

$$\begin{aligned} \mathrm{h}'(\xi) = \frac{\partial \boldsymbol{w}_{\mathrm{BF}k}^{\mathrm{H}}\left(\varphi_f\right)}{\partial\xi}\left(\boldsymbol{R}_F\left(\varphi_f\right)\boldsymbol{w}_{\mathrm{BF}k}\left(\varphi_f\right) - \boldsymbol{r}_{Fk}\left(\varphi_f\right)\right) \\ + \left(\boldsymbol{w}_{\mathrm{BF}k}^{\mathrm{H}}\left(\varphi_f\right)\boldsymbol{R}_F\left(\varphi_f\right) - \boldsymbol{r}_{Fk}^{\mathrm{H}}\left(\varphi_f\right)\right)\frac{\partial \boldsymbol{w}_{\mathrm{BF}k}\left(\varphi_f\right)}{\partial\xi} \end{aligned} \tag{A3}$$

Since $\boldsymbol{w}_{\mathrm{BF}k}\left(\varphi_f\right) = \left[\boldsymbol{R}_F\left(\varphi_f\right) + \frac{\xi}{\mathbf{w}_{0k}^{\mathrm{H}}\mathbf{w}_{0k}}\mathbf{I}\right]^{-1}\boldsymbol{r}_{Fk}\left(\varphi_f\right)$, the differential of $\boldsymbol{w}_{\mathrm{BF}k}\left(\varphi_f\right)$ to ξ is calculated as:

$$\frac{\partial \boldsymbol{w}_{\mathrm{BF}k}\left(\varphi_f\right)}{\partial\xi} = \frac{\partial\left(\left[\boldsymbol{R}_F\left(\varphi_f\right) + \frac{\xi}{\mathbf{w}_{0k}^{\mathrm{H}}\mathbf{w}_{0k}}\mathbf{I}\right]^{-1}\right)}{\partial\xi}\boldsymbol{r}_{Fk}\left(\varphi_f\right) \tag{A4}$$

Set

$$\boldsymbol{B} = \boldsymbol{R}_F\left(\varphi_f\right) + \frac{\xi}{\mathrm{P}_{\mathrm{w0}}}\mathbf{I} \tag{A5}$$

$$\mathrm{P}_{\mathrm{w0}} = \mathbf{w}_{0k}^{\mathrm{H}}\mathbf{w}_{0k}. \tag{A6}$$

Since $\frac{\partial \boldsymbol{B}^{-1}}{\partial\xi} = -\boldsymbol{B}^{-1}\frac{\partial \boldsymbol{B}}{\partial\xi}\boldsymbol{B}^{-1}$, $\frac{\partial \boldsymbol{w}_{\mathrm{BF}k}\left(\varphi_f\right)}{\partial\xi}$ can be written as:

$$\frac{\partial \boldsymbol{w}_{\mathrm{BF}k}\left(\varphi_f\right)}{\partial\xi} = -\boldsymbol{B}^{-1}\frac{\partial \boldsymbol{B}}{\partial\xi}\boldsymbol{B}^{-1}\boldsymbol{r}_{Fk}\left(\varphi_f\right) = -\frac{1}{\mathrm{P}_{\mathrm{w0}}}\boldsymbol{B}^{-2}\boldsymbol{r}_{Fk}\left(\varphi_f\right) \tag{A7}$$

Substitute $\frac{\partial \boldsymbol{w}_{\mathrm{BF}k}\left(\varphi_f\right)}{\partial \xi}$ above into $\mathrm{h}'(\xi)$ in (A3) to obtain

$$\begin{aligned}
&\mathrm{h}'(\xi)\\
&= -\tfrac{1}{\mathrm{P_{w0}}}\boldsymbol{r}_F^{\mathrm{H}}\left(\varphi_f\right)\boldsymbol{B}^{-2}\left(\boldsymbol{R}_F\left(\varphi_f\right)\boldsymbol{B}^{-1}\boldsymbol{r}_{Fk}\left(\varphi_f\right)-\boldsymbol{r}_{Fk}\left(\varphi_f\right)\right)\\
&\qquad -\tfrac{1}{\mathrm{P_{w0}}}\left(\boldsymbol{r}_{Fk}^{\mathrm{H}}\left(\varphi_f\right)\boldsymbol{B}^{-1}\boldsymbol{R}_F\left(\varphi_f\right)-\boldsymbol{r}_{Fk}^{\mathrm{H}}\left(\varphi_f\right)\right)\boldsymbol{B}^{-2}\boldsymbol{r}_F\left(\varphi_f\right)\\
&= -\tfrac{1}{\mathrm{P_{w0}}}\boldsymbol{r}_{Fk}^{\mathrm{H}}\left(\varphi_f\right)\boldsymbol{B}^{-2}\left(\boldsymbol{R}_F\left(\varphi_f\right)-\boldsymbol{B}\right)\boldsymbol{B}^{-1}\boldsymbol{r}_{Fk}\left(\varphi_f\right)\\
&\qquad -\tfrac{1}{\mathrm{P_{w0}}}\boldsymbol{r}_{Fk}^{\mathrm{H}}\left(\varphi_f\right)\boldsymbol{B}^{-1}\left(\boldsymbol{R}_F\left(\varphi_f\right)-\boldsymbol{B}\right)\boldsymbol{B}^{-2}\boldsymbol{r}_{Fk}\left(\varphi_f\right)\\
&= -\tfrac{1}{\mathrm{P_{w0}}}\boldsymbol{r}_{Fk}^{\mathrm{H}}\left(\varphi_f\right)\boldsymbol{B}^{-2}\left(-\tfrac{\xi}{\mathrm{P_{w0}}}\right)\boldsymbol{B}^{-1}\boldsymbol{r}_{Fk}\left(\varphi_f\right)-\tfrac{1}{\mathrm{P_{w0}}}\boldsymbol{r}_{Fk}^{\mathrm{H}}\left(\varphi_f\right)\boldsymbol{B}^{-1}\left(-\tfrac{\xi}{\mathrm{P_{w0}}}\right)\boldsymbol{B}^{-2}\boldsymbol{r}_{Fk}\left(\varphi_f\right)\\
&= \tfrac{2\xi}{\mathrm{P_{w0}^2}}\boldsymbol{r}_{Fk}^{\mathrm{H}}\left(\varphi_f\right)\boldsymbol{B}^{-3}\boldsymbol{r}_{Fk}\left(\varphi_f\right)
\end{aligned} \tag{A8}$$

Since $\boldsymbol{B}$ is a positive definite matrix, $\boldsymbol{r}_{Fk}^{\mathrm{H}}\left(\varphi_f\right)\boldsymbol{B}^{-3}\boldsymbol{r}_{Fk}\left(\varphi_f\right)>0$. Hence,
When $\xi=0$,

$$\mathrm{h}'(\xi)=0;$$

When $\xi=+\infty$

$$\begin{aligned}
h'(\xi) &= \tfrac{2\xi}{\mathrm{P_{w0}^2}}\boldsymbol{r}_{Fk}^{\mathrm{H}}\left(\varphi_f\right)\left[\boldsymbol{R}_F\left(\varphi_f\right)+\tfrac{\xi}{\mathrm{P_{w0}}}\mathbf{I}\right]^{-3}\boldsymbol{r}_{Fk}\left(\varphi_f\right)\\
&\approx \tfrac{2\mathrm{P_{w0}}}{\xi^2}\boldsymbol{r}_{Fk}^{\mathrm{H}}\left(\varphi_f\right)\boldsymbol{r}_{Fk}\left(\varphi_f\right)=0;
\end{aligned}$$

When $0<\xi<+\infty$

$$\mathrm{h}'(\xi)>0.$$

In conclusion, BSKF monotonically increases with respect to balance factor ξ.

Appendix B

The monotonicity of GNP with respect to balance factor ξ is demonstrated as follows:

Substitute the solution of $\boldsymbol{w}_{\mathrm{BF}k}\left(\varphi_f\right)$ in (23) into the definition of GNP in (18) to obtain the GNP with respect to the balance factor as:

$$\mathrm{g}(\xi)=\frac{\boldsymbol{w}_{\mathrm{BF}k}^{\mathrm{H}}\left(\varphi_f\right)\boldsymbol{w}_{\mathrm{BF}k}\left(\varphi_f\right)}{\mathrm{P_{w0}}}=\frac{\boldsymbol{r}_{Fk}^{\mathrm{H}}\left(\varphi_f\right)\boldsymbol{B}^{-2}\boldsymbol{r}_{Fk}\left(\varphi_f\right)}{\mathrm{P_{w0}}} \tag{A9}$$

Calculate the differential of $\mathrm{g}(\xi)$ with respect to ξ to obtain:

$$\mathrm{g}'(\xi)=\frac{\partial\left(\boldsymbol{r}_{Fk}^{\mathrm{H}}\left(\varphi_f\right)\boldsymbol{B}^{-2}\boldsymbol{r}_{Fk}\left(\varphi_f\right)\right)}{\mathrm{P_{w0}}\partial\xi}=\frac{\boldsymbol{r}_{Fk}^{\mathrm{H}}\left(\varphi_f\right)\partial\left(\boldsymbol{B}^{-2}\right)\boldsymbol{r}_{Fk}\left(\varphi_f\right)}{\mathrm{P_{w0}}\partial\xi} \tag{A10}$$

For matrix $\boldsymbol{B}$,

$$\boldsymbol{B}^{-2}=\left(\boldsymbol{B}^2\right)^{-1}. \tag{A11}$$

Set

$$\boldsymbol{C}=\boldsymbol{B}^2 \tag{A12}$$

Since $\frac{\partial \boldsymbol{C}^{-1}}{\partial\xi}=-\boldsymbol{C}^{-1}\frac{\partial \boldsymbol{C}}{\partial\xi}\boldsymbol{C}^{-1}$, $\mathrm{g}'(\xi)$ can be expanded into the following form

$$\begin{aligned}
\mathrm{g}'(\xi) &= \tfrac{1}{\mathrm{P_{w0}}}\boldsymbol{r}_{Fk}^{\mathrm{H}}\left(\varphi_f\right)(-1)\boldsymbol{C}^{-1}\tfrac{\partial \boldsymbol{C}}{\partial\xi}\boldsymbol{C}^{-1}\boldsymbol{r}_{Fk}\left(\varphi_f\right)\\
&= -\tfrac{1}{\mathrm{P_{w0}}}\boldsymbol{r}_{Fk}^{\mathrm{H}}\left(\varphi_f\right)\boldsymbol{B}^{-2}\left(\boldsymbol{B}\tfrac{\partial \boldsymbol{B}}{\partial\xi}+\tfrac{\partial \boldsymbol{B}}{\partial\xi}\boldsymbol{B}\right)\boldsymbol{B}^{-2}\boldsymbol{r}_{Fk}\left(\varphi_f\right)\\
&= -\tfrac{2}{\mathrm{P_{w0}^2}}\boldsymbol{r}_{Fk}^{\mathrm{H}}\left(\varphi_f\right)\boldsymbol{B}^{-3}\boldsymbol{r}_{Fk}\left(\varphi_f\right)
\end{aligned} \tag{A13}$$

Since $\boldsymbol{B}$ is a positive definite matrix, $\boldsymbol{r}_{Fk}^{\mathrm{H}}\left(\varphi_f\right)\boldsymbol{B}^{-3}\boldsymbol{r}_{Fk}\left(\varphi_f\right) > 0$. Hence,
When $\xi = 0$,

$$\mathrm{g}'(\xi) = -\frac{2}{\mathrm{P}_{\mathrm{w0}}^2}\boldsymbol{r}_{Fk}^{\mathrm{H}}\left(\varphi_f\right)\left[\boldsymbol{R}_F\left(\varphi_f\right)\right]^{-3}\boldsymbol{r}_{Fk}\left(\varphi_f\right) < 0;$$

When $\xi = +\infty$

$$\begin{aligned} g'(\xi) &= -\tfrac{2}{\mathrm{P}_{\mathrm{w0}}^2}\boldsymbol{r}_{Fk}^{\mathrm{H}}\left(\varphi_f\right)\left[\boldsymbol{R}_F\left(\varphi_f\right) + \tfrac{\xi}{\mathrm{P}_{\mathrm{w0}}}\mathbf{I}\right]^{-3}\boldsymbol{r}_{Fk}\left(\varphi_f\right) \\ &\approx -\tfrac{2\mathrm{P}_{\mathrm{w0}}}{\xi^3}\boldsymbol{r}_{Fk}^{\mathrm{H}}\left(\varphi_f\right)\boldsymbol{r}_{Fk}\left(\varphi_f\right) = 0; \end{aligned}$$

When $0 < \xi < +\infty$

$$\mathrm{g}'(\xi) < 0.$$

In conclusion, GNP monotonically decreases with respect to balance factor ξ.

References

1. Li, M.; Zhang, L.; Wu, X.; Yue, X.; Emery, W.J.; Yi, X.; Liu, J.; Yang, G. Ocean Surface Current Extraction Scheme with High-Frequency Distributed Hybrid Sky-Surface Wave Radar System. *IEEE Trans. Geosci. Remote Sens.* **2018**, *56*, 4678–4690. [CrossRef]
2. Saviano, S.; Kalampokis, A.; Zambianchi, E.; Uttieri, M. A year-long assessment of wave measurements retrieved from an HF radar network in the Gulf of Naples (Tyrrhenian Sea, Western Mediterranean Sea). *J. Oper. Oceanogr.* **2019**, *12*, 1–15. [CrossRef]
3. Orasi, A.; Picone, M.; Drago, A.; Capodici, F.; Gauci, A.; Nardone, G.; Inghilesi, R.; Azzopardi, J.; Galea, A.; Ciraolo, G.; et al. HF radar for wind waves measurements in the Malta-Sicily Channel. *Measurement* **2018**, *128*, 446–454. [CrossRef]
4. Fang, H.; Xie, T.; Perrie, W.; Zhao, L.; Yang, J.; He, Y. Ocean Wind and Current Retrievals Based on Satellite SAR Measurements in Conjunction with Buoy and HF Radar Data. *Remote Sens.* **2017**, *9*, 1321. [CrossRef]
5. Hisaki, Y. Sea Surface Wind Correction Using HF Ocean Radar and Its Impact on Coastal Wave Prediction. *J. Atmos. Ocean. Technol.* **2017**, *34*, 2001–2020. [CrossRef]
6. Yang, Z.; Zhou, H.; Tian, Y.; Zhao, J. Improved CFAR Detection and Direction Finding on Time-Frequency Plane with High-Frequency Radar. *IEEE Geosci. Remote Sens.* **2022**, *19*, 3505005. [CrossRef]
7. Chuang, L.Z.; Chen, Y.; Chung, Y. Applying an Adaptive Signal Identification Method to Improve Vessel Echo Detection and Tracking for SeaSonde HF Radar. *Remote Sens.* **2021**, *13*, 2453. [CrossRef]
8. Nikolic, D.; Stojkovic, N.; Popovic, Z.; Tosic, N.; Lekic, N.; Stankovic, Z.; Doncov, N. Maritime Over the Horizon Sensor Integration: HFSWR Data Fusion Algorithm. *Remote Sens.* **2019**, *11*, 852. [CrossRef]
9. Khoury, J.E.; Guinvarc'H, R.; Gillard, R.; Uguen, B. Sea-echo doppler spectrum perturbation of the received signals from a floating high-frequency surface wave radar. *IET Radar Sonar Navig.* **2012**, *6*, 165–171. [CrossRef]
10. Xie, J.; Yuan, Y.; Liu, Y. Experimental analysis of sea clutter in shipborne HFSWR. *IEE Proc.-Radar Sonar Navig.* **2001**, *148*, 67–71. [CrossRef]
11. Walsh, J.; Huang, W.; Gill, E. The First-Order High Frequency Radar Ocean Surface Cross Section for an Antenna on a Floating Platform. *IEEE Trans. Antenn. Propag.* **2010**, *58*, 2994–3003. [CrossRef]
12. Yao, G.; Xie, J.; Huang, W. Ocean Surface Cross Section for Bistatic HF Radar Incorporating a Six DOF Oscillation Motion Model. *Remote Sens.* **2019**, *11*, 2738. [CrossRef]
13. Yi, X.; Wu, X.; Yue, X.; Zhang, L.; Chen, Z.; Wan, B. Ocean Surface Current Inversion with Anchored Floating High-Frequency Radar: Yaw Compensation. *IEEE J. Ocean. Eng.* **2021**, *46*, 927–939. [CrossRef]
14. Yang, K.; Zhang, L.; Niu, J.; Ji, Y.; Wu, Q.M.J. Analysis and Estimation of Shipborne HFSWR Target Parameters Under the Influence of Platform Motion. *IEEE Trans. Geosci. Remote. Sens.* **2021**, *59*, 4703–4716. [CrossRef]
15. Shi, C.; Zhang, L.; Niu, J.; Wu, M.; Zhang, J. DOA Estimation for Shipborne HFSWR: Model and Analysis. In Proceedings of the OCEANS 2021, San Diego–Porto:MTS, San Diego, CA, USA, 20–23 September 2021; pp. 1–4.
16. Yi, X. Three DOF Rotation Compensation in Floating HFSWR for Ocean Current Inversion. *J. Phys. Conf. Ser.* **2024**, *2718*, 12017.
17. Wang, C.; Zhang, L.; Niu, J.; Li, G.; Wu, Q.M.J. Accurate Direction Finding for Shipborne HFSWR Through Platform Motion Compensation. *IEEE Trans. Geosci. Remote Sens.* **2023**, *61*, 5110917.
18. Ji, Y.; Wang, Y.; Huang, W.; Sun, W.; Zhang, J.; Li, M.; Cheng, X. Vessel Target Echo Characteristics and Motion Compensation for Shipborne HFSWR under Non-Uniform Linear Motion. *Remote Sens.* **2021**, *13*, 2826. [CrossRef]
19. Stoica, P.; Nehorai, A. MUSIC, maximum likelihood, and Cramer-Rao bound: Further results and comparisons. *IEEE Trans. Acoust. Speech Signal Process.* **1990**, *38*, 2140–2150.

20. Tirer, T.; Weiss, A.J. High Resolution Direct Position Determination of Radio Frequency Sources. *IEEE Signal Process. Lett.* **2016**, *23*, 192–196.
21. Yi, X.; Wu, X.; Wan, B.; Li, Z. Analysis of Direction-of-Arrival Estimation for a Floating High-Frequency Radar with Yaw Rotation. *IEEE J. Ocean. Eng.* **2024**, *49*, 1183–1198.
22. Wan, B.; Wu, X.; Yue, X.; Zhang, L.; Wang, L. Calibration of Phased-Array High-Frequency Radar on an Anchored Floating Platform. *Remote Sens.* **2022**, *14*, 2174. [CrossRef]
23. Yang, S.; Ke, H.; Wu, X.; Tian, J.; Hou, J. HF radar ocean current algorithm based on MUSIC and the validation experiments. *IEEE J. Ocean. Eng.* **2005**, *30*, 601–618.
24. Chen, Z.; He, C.; Zhao, C.; Xie, F. Enhanced Target Detection for HFSWR by 2-D MUSIC Based on Sparse Recovery. *IEEE Geosci. Remote Sens.* **2017**, *14*, 1983–1987.
25. Xu, Z.; Tang, B.; Ai, W.; Zhu, J. Relative Entropy Based Jamming Signal Design Against Radar Target Detection. *IEEE Trans. Signal Process.* **2025**, *73*, 1200–1215. [CrossRef]
26. Zhu, J.; Yin, T.; Guo, W.; Zhang, B.; Zhou, Z. An Underwater Target Azimuth Trajectory Enhancement Approach in BTR. *Appl. Acoust.* **2025**, *230*, 110373.
27. Yin, T.; Guo, W.; Zhu, J.; Wu, Y.; Zhang, B.; Zhou, Z. Underwater Broadband Target Detection by Filtering Scanning Azimuths Based on Features of Sub-band Peaks. *IEEE Sens. J.* **2025**. [CrossRef]

Disclaimer/Publisher's Note: The statements, opinions and data contained in all publications are solely those of the individual author(s) and contributor(s) and not of MDPI and/or the editor(s). MDPI and/or the editor(s) disclaim responsibility for any injury to people or property resulting from any ideas, methods, instructions or products referred to in the content.